Since January 2020 Elsevier has created a COVID-19 resource centre with free information in English and Mandarin on the novel coronavirus COVID-19. The COVID-19 resource centre is hosted on Elsevier Connect, the company's public news and information website.

Biosensors and Bioelectronics 237 (2023) 115457

Contents lists available at ScienceDirect

Biosensors and Bioelectronics

journal homepage: www.elsevier.com/locate/bios

Antibody- and aptamer-free SERS substrate for ultrasensitive and anti-interference detection of SARS-CoV-2 spike protein in untreated saliva

Hong Zhang [a], Chenggang Zhang [a], Zhaotong Wang [a], Wenwu Cao [a], Miao Yu [b,*], Ye Sun [a,**]

[a] School of Instrumentation Science and Engineering, Harbin Institute of Technology, Harbin, 150001, Heilongjiang, PR China
[b] State Key Laboratory of Urban Water Resource and Environment, School of Chemistry and Chemical Engineering, Harbin Institute of Technology, Harbin, 150001, Heilongjiang, PR China

ARTICLE INFO

Keywords:
SARS-CoV-2 spike protein
Antibody/aptamer-free
Biosensor
SERS
Untreated saliva

ABSTRACT

Sensitive and anti-interference detection of targeted signal(s) in body fluids is one of the paramount tasks in biosensing. Overcoming the complication and high cost of antibody/aptamer-modification, surface-enhanced Raman spectroscopy (SERS) based on antibody/aptamer-free (AAF) substrates has shown great promise, yet with rather limited detection sensitivity. Herein, we report ultrasensitive and anti-interference detection of SARS-CoV-2 spike protein in untreated saliva by an AAF SERS substrate, applying the evanescent field induced by the high-order waveguide modes of well-defined nanorods for SERS for the first time. A detection limit of 3.6×10^{-17} M and 1.6×10^{-16} M are obtained in phosphate buffered saline and untreated saliva, respectively; the detection limits are three orders of magnitude improved than the best records from AAF substrates. This work unlocks an exciting path to design AAF SERS substrates for ultrasensitive biosensing, not limited to detection of viral antigens.

1. Introduction

Sensitive and anti-interference detection of targeted molecules/proteins in body fluids (*e.g.*, saliva, urine and blood) is one of the paramount tasks in biosensing (Fiedorova et al., 2022; Ohayon et al., 2020; Shen et al., 2021; Li et al., 2021). In the context of the global pandemic of SARS-CoV-2 and its variants, sensitive detection of highly pathogenic viruses has shown pressing importance in screening patients hence controlling the mass spread (Cui and Zhou, 2020; Lukose et al., 2021; Taleghani and Taghipour, 2021). Superior to the nucleic acid detection which has high requirements for instrument, laboratory cleanliness and sample storage/transfer conditions and the antibody detection which is not suitable for screening early infection as the generation of specific antibodies in blood often takes a week or longer (Kevadiya et al., 2021; Weissleder et al., 2020), detection of viral antigens is more convenient and time-efficient (Yüce et al., 2021; Singh et al., 2021; Vecchio et al., 2022). A big variety of viral antigen detection kits using immunoassay technologies have been developed (Pavia and Plummer, 2021); nevertheless, as SARS-CoV-2 mainly invades the lower respiratory tract (*e.g.*, alveoli), the virus content collected from nasopharynx or oropharynx for the antigens detection is rather limited yet with the interference of body fluids, inducing a high false negative rate (Parvu et al., 2021; Mak et al., 2022). Achieving high sensitivity and accuracy of low-concentration viral antigens in body fluids is still highly challenging.

Based on the fingerprint effect of molecules and largely-improved signal intensity, surface-enhanced Raman spectroscopy (SERS) has demonstrated remarkable potential on the ultrahigh sensitive detection of biological targets, ranging from a single molecule to a single cell (Chang et al., 2022; Xiong et al., 2022; Antoine et al., 2022; Zhang et al., 2022). Recently, SERS detection of SARS-CoV-2 spike protein has stimulated intense attention (Zhang et al., 2021; Gu et al., 2023; Stanborough et al., 2021; Yeh et al., 2023). To improve the detection sensitivity, a common strategy is to modify the SERS substrate by SARS-CoV-2 spike antibody or oligonucleotide aptamers (Zhang et al., 2021; Gu et al., 2023; Stanborough et al., 2021; Yeh et al., 2023). For example, by employing the antibody-modified SERS substrate and 4-mercaptobenzoic acid as Raman reporter, Lu et al. successfully delivered a detection record of 1.1×10^{-17} mol·L^{-1} (M) in phosphate buffered saline (PBS) and 8.6×10^{-17} M in untreated saliva, respectively (Zhang et al., 2021). Still, the complicated, high-cost modification of such SERS substrates restricts their real-life applications. Enormous

* Corresponding author. 92 Xidazhi Street, Harbin, 150001, China.
** Corresponding author. 92 Xidazhi Street, Harbin, 150001, China.
E-mail addresses: miaoyu_che@hit.edu.cn (M. Yu), sunye@hit.edu.cn (Y. Sun).

https://doi.org/10.1016/j.bios.2023.115457
Received 17 March 2023; Received in revised form 12 May 2023; Accepted 7 June 2023
Available online 8 June 2023

efforts have been devoted to design antibody/aptamer-free SERS substrates (Wu et al., 2022; Zhang et al., 2023; Luo et al., 2023; Peng et al., 2021; Daoudi et al., 2021); however, the detection sensitivity has been rather limited: the best detection limit so far has been only 1.3×10^{-13} M in PBS by using a SERS substrate based on bowtie nanoaperture arrays with metal-insulator-metal configuration (Luo et al., 2023). Due to the complex composition of saliva hence strong interference to the target signals, detection of saliva's protein is much more challenging: the detection limit could be one or two orders of magnitude poorer than that in PBS (Zhang et al., 2021; Stanborough et al., 2021). As the cutting-edge goal of biosensing has reached the femto-molar (10^{-15} M) or even atto-molar (10^{-18} M) level (Macchia et al., 2022; Zhang et al., 2020), developing antibody/aptamer-free and anti-interference SERS substrates with substantially-improved detection limit is, therefore, highly desirable.

Herein, we report ultrasensitive and anti-interference detection of SARS-CoV-2 spike protein in untreated saliva by antibody/aptamer-free SERS substrate. As illustrated in Scheme 1, we construct vertically-aligned zinc oxide nanorods (ZnO NRs) arrays on a silver (Ag) film, and decorate the NRs' sidewalls with 2-mercaptoethanol (MET, C_2H_6OS) ligands-covered gold nanoparticles (Au NPs). Both the diameter-optimized ZnO NRs with bare top and highly-reflective Ag film are employed to strengthen the evanescent field outside the ZnO NRs (Voss et al., 2007; Börner et al., 2007; Du et al., 2019; Yin et al., 2015) and thus to enhance the excitation of Au NPs for SERS detection. MET coating on the Au NPs can effectively capture SARS-CoV-2 and reduce the interference of salivary signal. As a result, a detection limit of 3.6×10^{-17} M in PBS and of 1.6×10^{-16} M in untreated saliva are obtained for SARS-CoV-2 spike protein, respectively; the detection limits are three orders of magnitude improved than the best detection limit from antibody/aptamer-free SERS substrates ever reported (Wu et al., 2022; Luo et al., 2023). This work unlocks a fascinating path for design of antibody/aptamer-free SERS substrates for ultrasensitive, anti-interference detection of SARS-CoV-2 spike protein in untreated saliva, and the high detection capability emphasizes great promise for diverse biosensing, not limited to detection of viral antigens.

2. Materials and methods

2.1. Chemicals

zinc nitrate hexahydrate [ZNH, $Zn(NO_3)_2{\cdot}6H_2O$], hexamethylenetetramine (HMT, $C_6H_{12}N_4$), gold (III) chloride trihydrate ($HAuCl_4{\cdot}3H_2O$), sodium borohydride ($NaBH_4$), sodium hydroxide (NaOH), MET, rhodamine 6G (R6G) were purchased from Aladdin Reagent Co. Ltd (China). SARS-CoV-2 spike protein (molecular weight of 70 kDa) was ordered from MerryBio Co. Ltd. (China). PBS buffer (0.01 M, pH 7.4) was purchased from Biotopped Co. Ltd. (China). All chemicals were of analytical grade and used as received. Deionized water (resistivity of 18.2 MΩ cm) was used in all experiments.

2.2. Instruments

The samples were characterized by scanning electron microscopy (SEM, FEI, Quanta 200FEG), high-resolution transmission electron microscopy (HRTEM, FEI, Tecnai G2 F30) equipped with energy dispersive X-ray spectrometer (EDS), and X-ray diffraction (XRD, PANalytical, X'Pert Pro) using a diffractometer with Cu Kα as the radiation source and X-ray photoelectron spectroscopy (XPS, Thermo Fisher Scientific, ESCALAB250Xi). Raman spectra were collected using a Raman spectrometer (Horiba, LabRAM HR Evolution).

2.3. Fabrication of the SERS substrates

The Ag film was deposited on a Si substrate in vacuum at room temperature by a radio-frequency (RF) magnetron sputtering method with RF power of 100 W. Next, the ZnO seed layer was deposited on the Ag film at room temperature in an oxygen (O_2)/argon (Ar) atmosphere (at a pressure of 1 Pa with O_2 flow rate of 10 sccm and Ar flow rate of 40 sccm with RF power of 150 W). Vertically-aligned ZnO NR arrays were then grown on the seed layer: ZNH solution (50 mL) and HMT solution (50 mL) were heated separately to 90 °C in water bath for 30 min and then mixed together in a glass bottle. After immersing the ZnO seed-coated Ag film substrate in the solution, the glass bottle was sealed and maintained at 90 °C for 3 h. The obtained samples were then taken

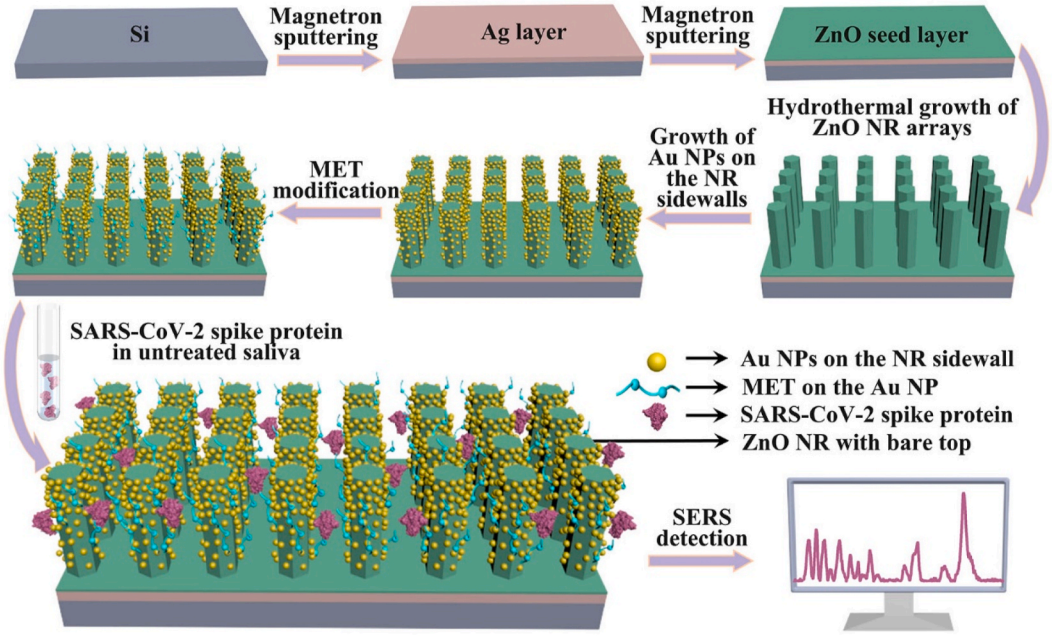

Scheme 1. Illustration for the SERS substrate fabrication. The fabrication process involves i) deposition of an Ag film and a ZnO seed layer on a silicon (Si) wafer, ii) growth of the vertically-aligned ZnO NRs arrays on the seed layer, iii) selective decoration of the Au NPs on the sidewalls of the ZnO NRs, and iv) MET-modification of the Au NPs' surface.

out of the solution, rinsed with deionized water and dried with nitrogen gas. By changing concentrations of the ZNH and HMT solution in the range of 0.15–0.30 M, the diameter of the ZnO NRs can be modified. Employing a modified successive ionic layer adsorption and reaction (SILAR) method, Au NPs were selectively grown on the sidewalls of the ZnO NRs. Briefly, the samples (ZnO NRs grown on the Ag film-Si wafer) were first immersed in $HAuCl_4{\cdot}3H_2O$ solution (10 mM) for 2 min, immersed in $NaBH_4$ solution (10 mM) for 2 min, and then rinsed with deionized water to remove the unreacted residues. Such process was called one SILAR cycle. Based on the investigation of the influence of SILAR cycles on growth of Au NPs, four SILAR cycles were finally selected as the optimized setting. MET was finally employed to modify the surface of the Au NPs. MET (7.813 μg) was dissolved in deionized water (10 mL). After immersing in the MET solution at 4 °C for 30 min, the samples were rinsed with deionized water for three times to remove excess MET.

2.4. Evaluation of SERS enhancement and detection of SARS-CoV-2 spike protein

R6G was used as probe to investigate the detection performance of the obtained SERS substrate. The *A1*–*A5* substrates were immersed in R6G aqueous solution (10 mL) at various concentrations (10^{-5}–10^{-17} M) for 24 h. The substrates were then taken out and dried with nitrogen gas. The SERS spectra of R6G were collected upon 532 nm laser excitation (laser power of 10 mW prior to lens, two accumulations at 10 s acquisition time) and 785 nm laser excitation (laser power of 10 mW prior to lens, two accumulations at 10 s acquisition time). For SERS detection of SARS-CoV-2 spike protein, SARS-CoV-2 spike protein (1 $mg{\cdot}mL^{-1}$, 20 μL) was dissolved in PBS (1.5 mL), then diluted in PBS to obtain various concentrations (10^{-7}–10^{-15} M) or diluted in untreated saliva to obtain various concentrations (10^{-9}–10^{-15} M). The saliva was collected from healthy volunteers after rinsing their mouths three times with deionized water. All the related experiments were permitted by relevant laws and complied with institutional ethical guidelines, and all the healthy volunteers agreed to participate in this study. The SERS substrates with/without MET modification were immersed in spike protein solution at 4 °C for 1 h, and then washed using PBS solution and dried with a stream of nitrogen. The temperature of 4 °C is a commonly-used temperature to maintain the structural integrity of proteins (Yeh et al., 2023; Bistaffa et al., 2022; Johnson, 2012). The SERS detection of SARS-CoV-2 spike protein was performed upon 785 nm excitation (laser power of 10 mW prior to lens, two accumulations at 15 s acquisition time). All SERS spectra were background-corrected and analyzed using the LabSpec6 software (Horiba).

2.5. Principal component analysis (PCA)

PCA was performed employing Scikit-Learn (sklearn) Library running under Python 3.8.5 environment. Each set of background-corrected Raman spectra for PCA contained 40 datasets. For each SERS spectrum, 1847 variables were selected from Raman shifts in the range of 550~1800 cm^{-1}. The first and second principal components were used for data analysis.

3. Results

3.1. Fabrication and characterization of the SERS substrates

To fabricate the SERS substrates, an Ag film with an average thickness of ~660 nm (Fig. S1a) was first deposited on a Si wafer. Based on the XRD pattern (Fig. S1b) and diffuse reflectance spectra (Fig. S1c), the Ag film had high crystallinity and high light reflection. Following deposition of the ZnO seed layer (thickness of ~20 nm) on the Ag film, vertical-aligned ZnO NRs arrays were grown on the seed layer using a hydrothermal method. By changing the concentrations of precursor, *i.e.*, ZNH, and HMT solution, the average diameter of the ZnO NRs can be varied in a controlled manner. We constructed five ZnO NRs arrays on the Ag film with different average diameters of the NRs, named as '*A1*', '*A2*', '*A3*', '*A4*', and '*A5*', respectively. As seen from the top-view and cross-sectional SEM images of the five NRs samples (Fig. 1a–e), the vertically-aligned ZnO NRs had a typical hexagonal prism morphology, indicating their good crystal quality and *c*-axis alignment. The crystallinity and growth orientation of the NRs were confirmed by the XRD pattern (Fig. S1d). From the statistical analysis of the SEM results, the NRs' average diameters of *A1*–*A5* samples (Fig. S2) were ~155, 205, 240, 349 and 435 nm, and the NRs' average lengths (Fig. 1a–e) were ~1.3, 1.3, 1.2, 1.1 and 1.1 μm, respectively.

Next, decorating Au NPs on the *A1*–*A5* NRs by a modified SILAR method (Kim et al., 2018), we obtained the samples of '*A1@Au*'–'*A5@Au*'. As shown in Fig. 2a–e, the Au NPs were selectively grown on the ZnO NRs' sidewalls, keeping the NRs' top surface bare. Using HRTEM image of *A4@Au* sample as an example, two sets of inter-planar spacing were revealed, *i.e.*, ~0.26 and 0.23 nm (Fig. 2f), which are characteristics of ZnO(002) (along *c*-axis) and Au(111) planes.

To further confirm the successful introduction of Au NPs, the composition of the samples were analyzed by XPS. As shown in Fig. S3, the presence of Zn, O and Au elements can be clearly identified; the peaks located at 1021.2, 1044.3, 88.8 and 91.6 eV belonged to Zn $2p_{3/2}$, $2p_{1/2}$, $3p_{3/2}$ and $3p_{1/2}$, respectively; the two O *1s* peaks (530.4 eV and 531.7 eV) corresponded to the binding of O to Zn in ZnO NRs and oxygen vacancies, respectively; the two peaks at 83.7 and 87.3 eV were attributed to $4f_{7/2}$ and $4f_{5/2}$ of metallic Au.

3.2. SERS detection using the pristine substrates

To avoid the interference of fluorescence signal associated with the complex substances in saliva, we used 785 nm excitation wavelength for SERS detection of SARS-CoV-2 spike protein. The detection performance of the pristine substrates *A1@Au*, *A2@Au*, *A3@Au*, *A4@Au* and *A5@Au* was first investigated using R6G as probe. As shown in Fig. 3a, after treated by R6G solution (10^{-5} M), typical spectral features of R6G were identified from all the five substrates. As summarized in Table S1, the peaks located at 612, 773, 1362, and 1570 cm^{-1} were attributed to C–C–C ring in-plane vibrations, C–H out-of-plane bending vibrations, symmetric C–C in-plane stretching vibrations, and aromatic C–C stretching vibrations, respectively. The peak intensity at 612 cm^{-1} (I_{612}) indicated that the detection capability can vary with the ZnO NRs' diameter (Fig. 3b); *A4@Au* exhibited the best SERS performance superior to the rest substrates. *A4@Au* was then used as the SERS substrate to detect SARS-CoV-2 spike protein in PBS (10^{-7} M) upon 785 nm excitation. Distinct from the control group (pure PBS on *A4@Au*) showing barely any noticeable Raman peaks, representative vibrational bands of SARS-CoV-2 spike protein can be clearly identified at 680, 771, 821, 887, 935, 1162, 1217, 1260, 1289, 1565 cm^{-1} (Fig. 3c), corresponding to C–H deformation vibration of tryptophan, aromatic/indole ring stretching vibration of phenylalanine, hydroxyphenyl ring of tyrosine, N–H stretching vibrations of tryptophan, C–C and C–N stretching vibrations of the skeleton, C–C stretching vibrations of tyrosine, phenylalanine, α-helix amide III, and indole ring of tryptophan, respectively (Table S2).

Although the pristine substrates worked well for detection of both R6G in deionized water and SARS-CoV-2 spike protein in PBS, detection of viral protein in untreated saliva was much more challenging due to the complex composition of saliva. When detecting SARS-CoV-2 spike protein in untreated saliva using *A4@Au* SERS substrate (Fig. 3d), instead of showing any noticeable signals of SARS-CoV-2 spike protein, all the identified Raman bands were indexed to the organic compounds of untreated saliva (Table S3): the peaks located at 730, 885, 1134, 1446, and 1660 cm^{-1} correspond to mucin; those at 813, 1002, 1205, 1244, 1270, 1320, and 1446 cm^{-1} are attributed to collagen; those at

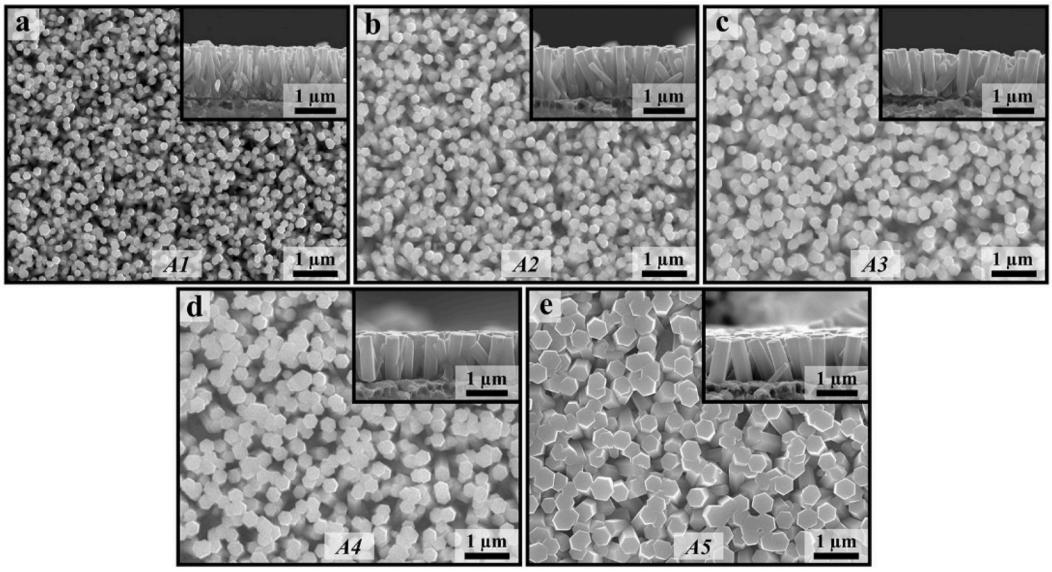

Fig. 1. Morphology of the ZnO NRs arrays. Top-view (main panel) and cross-sectional (inset) SEM images of (a) *A1*, (b) *A2*, (c) *A3*, (d) *A4*, and (e) *A5* samples, revealing the typical hexagonal prism morphology of the NRs and the average diameter of ~155, 205, 240, 349 and 435 nm for *A1–A5* NRs, respectively.

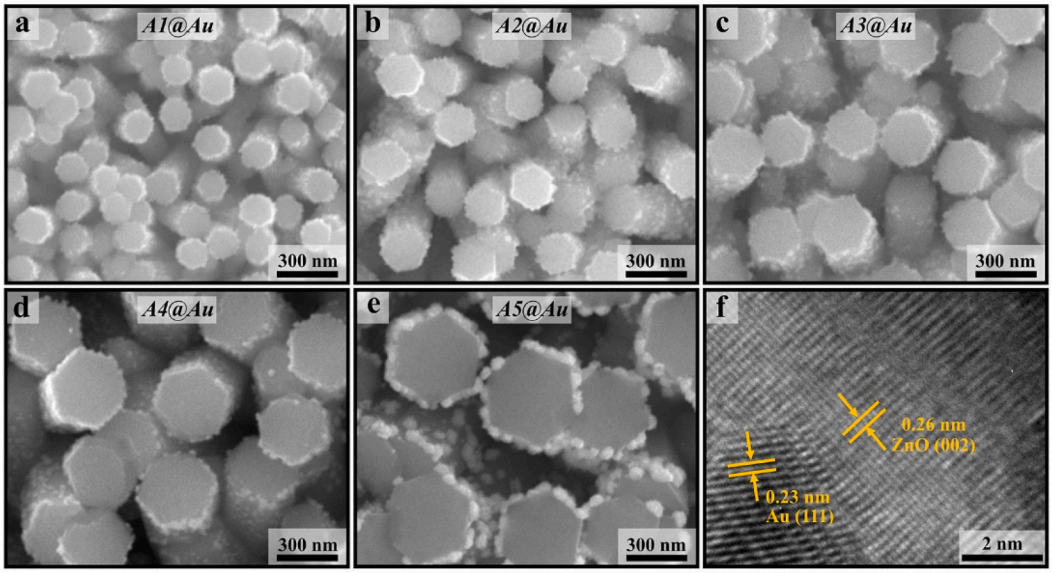

Fig. 2. Morphology of the arrays after decoration of the Au NPs. Top-view SEM images of (a) *A1@Au*, (b) *A2@Au*, (c) *A3@Au*, (d) *A4@Au*, and (e) *A5@Au*, showing the selective decoration of the Au NPs on the sidewalls of the NRs. (f) HRTEM image of *A4@Au*, where both the ZnO NRs and the attached Au NPs show high crystalline.

1205 and 1588 cm^{-1} belong to phenylalanine; and those at 648, 683, 962, 1002, and 1205 cm^{-1} are corresponding to tyrosine, cysteine, proline-rich protein, amylase, and tryptophan, respectively. The fine detection for SARS-CoV-2 spike protein in PBS but poor performance in untreated saliva suggested the insufficient spike-protein capturing capability of the pristine substrate upon the interference of various organic compounds in untreated saliva.

3.3. MET-modified substrate improving the detection selectivity in untreated saliva

To promote the spike-protein capturing capability, MET was employed to modify the Au NPs' surface of the pristine SERS substrates. We first evaluated SERS detection of SARS-CoV-2 spike protein in PBS (10^{-7} M) by using MET-modified *A4@Au* (denoted by *A4@MET-Au*) substrate. Evidently, the SERS spectrum showed strong vibration signals of SARS-CoV-2 spike protein (Fig. 4a). Additional peaks associated with MET were also observed, where the peaks located at 637, 726, 935, 1016, 1049, 1212, and 1276 cm^{-1} are attributed to C–S stretching vibrations of the gauche conformer, C–S stretching vibrations of the trans conformer, C–C stretching vibrations of the trans conformer, C–C–O out-of-phase stretching vibrations, C–C stretching vibrations of the trans conformer, CH_2 twisting and CH_2 wagging, respectively (Table S4).

We then evaluated the detection capability of SARS-CoV-2 spike protein in untreated saliva (10^{-12} M) using *A4@MET-Au* SERS substrate. Remarkably, distinct from the case of *A4@Au*, after MET modification, significant vibration signals corresponding to SARS-CoV-2 spike protein (located at 680, 771, 887 and 1565 cm^{-1}) were observed together with the MET peaks (Fig. 4b); no vibrations associated with saliva were observed. As the representative peaks of SARS-CoV-2 spike protein, *e.g.*,

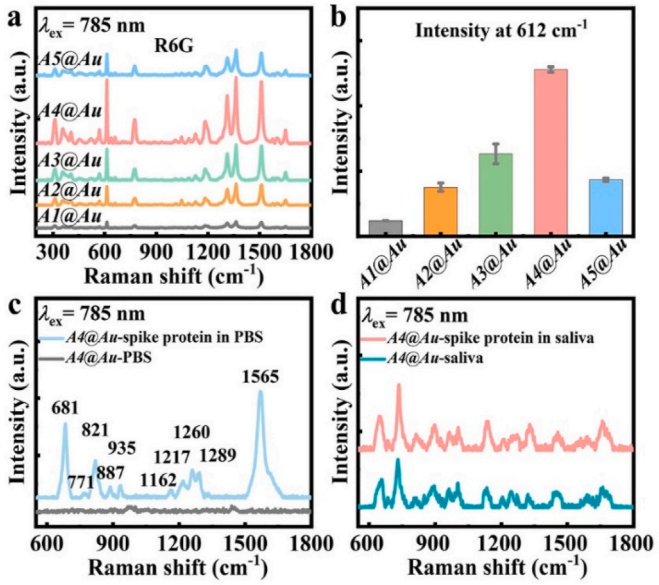

Fig. 3. SERS detection performance of the pristine substrates. (a) SERS spectra collected from the pristine *A1–A5@Au* SERS substrates treated by R6G solution (10^{-5} M) upon 785 nm excitation. (b) The intensity recorded at 612 cm^{-1}, indicating that *A4@Au* has the best detection performance. Each error bar indicates the standard deviation of five different measurements from a single SERS substrate. (c) SERS spectrum of SARS-CoV-2 spike protein in PBS (10^{-7} M), using *A4@Au* as the substrate and the spectrum of pure PBS on *A4@Au* as control. (d) SERS spectrum of SARS-CoV-2 spike protein in untreated saliva (10^{-12} M) using *A4@Au* as the substrate, compared with the spectrum of untreated saliva.

the one at 680 cm^{-1}, were not interfered by the signals of MET, effective detection for SARS-CoV-2 spike protein was enabled.

To explore the detection limit, SERS spectra of SARS-CoV-2 spike protein at various concentrations in PBS (Fig. 4c) and in untreated saliva (Fig. 4d) were collected, using *A4@MET-Au* as SERS substrate. In both cases, the vibration signal at 680 cm^{-1} associated with SARS-CoV-2 spike protein can be identified down to a low concentration of 10^{-15} M. Based on the linear correlation plot of *log*(I_{680}) *vs. log*(the protein concentration) (Fig. 4e and f), the detection limit of *A4@MET-Au* for SARS-CoV-2 spike protein in PBS and untreated saliva was determined to be 3.6 × 10^{-17} M and 1.6 ×10^{-16} M, respectively, following the International Union of Pure and Applied Chemistry standard method (Long and Winefordner, 1983) which has been commonly applied (Zhang et al., 2021; Wu et al., 2022; Luo et al., 2023). Compared with the best antibody/aptamer-free SERS detection records reported previously, *i.e.,* 1.3 × 10^{-13} M in PBS using a SERS substrate of bowtie nanoaperture arrays with metal-insulator-metal configuration (Luo et al., 2023) and 5.6 × 10^{-13} M in saliva using a SERS substrate of Au nanoplate film/MgF_2/Au mirror/glass (Wu et al., 2022), the present detection limits were improved at least three orders of magnitude.

4. Discussion

The ultrasensitive and anti-interference detection of SARS-CoV-2 spike protein in untreated saliva using *A4@MET-Au* can be attributed to two major contributions: i) the significant evanescent field induced by the diameter-optimized ZnO NRs on Ag film; ii) selectively capturing of SARS-CoV-2 spike protein upon the interference of saliva enabled by MET modification.

It has been well demonstrated that higher-order waveguide modes of ZnO NRs can provide a NR-diameter-dependent evanescent field outside the NRs; the direction of the evanescent field is perpendicular to the *c*-axis of the NRs (Voss et al., 2007; Börner et al., 2007; Du et al., 2019). SERS is essentially based on the electromagnetic enhancement induced by the coupling between the incident light and the localized surface plasmon resonance (LSPR) of the noble metal NPs , where the LSPR-associated electromagnetic enhancement of these NPs is dependent on the intensity of the excitation light (Wang et al., 2020; Ding et al., 2016). The evanescent field of the NRs can effectively promote the excitation of the Au NPs on the NRs' sidewalls. Moreover, the bare top of the ZnO NRs benefits the entrance of radiation light into the NRs; the light-reflection Ag film beneath the NRs further enhances the evanescent

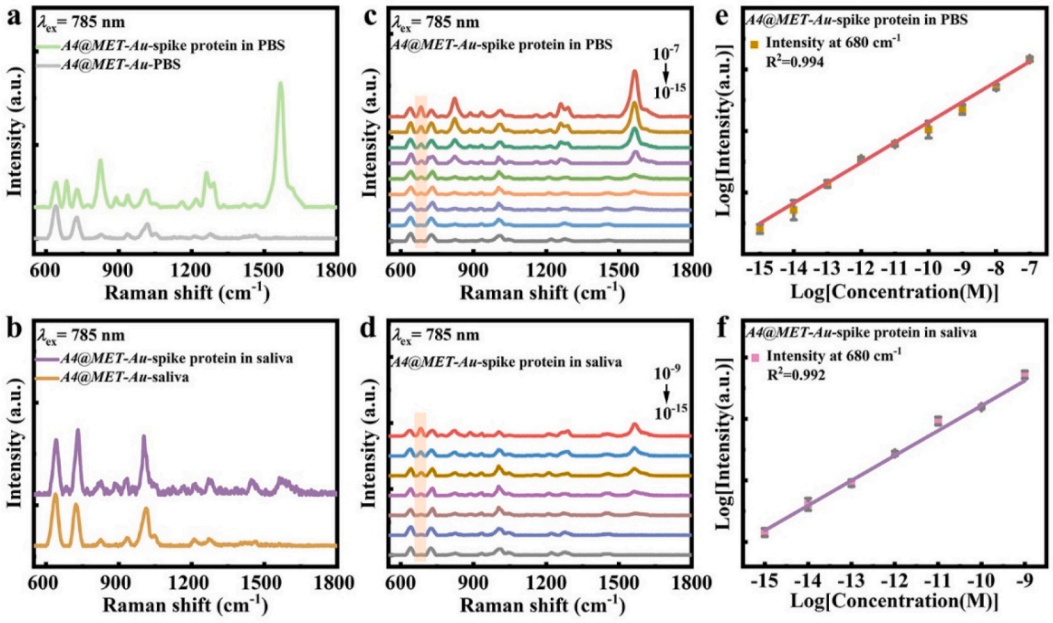

Fig. 4. Detection of SARS-CoV-2 spike protein using *A4@MET-Au* substrate. SERS spectra of SARS-CoV-2 spike protein (a) in PBS (with pure PBS as control), (b) in untreated saliva (10^{-12} M, with virus-free saliva as control), (c) in PBS at various concentrations of the spike protein (10^{-7}–10^{-15} M), and (d) in untreated saliva at various concentrations of the spike protein (10^{-9}–10^{-15} M). Evolution curve of the *log*(I_{680}) *vs. log*(SARS-CoV-2 spike protein concentration) (e) derived from panel c and (f) derived from panel d, respectively. Each error bar indicates the standard deviation of five different measurements from a single SERS substrate.

field and reduces the absorption of the excitation light and SERS signal by the Si wafer.

To intuitively compare the evanescent field of *A1–A5@Au*, we carried out finite difference time domain (FDTD) simulations for ZnO NRs with five different diameters on the Ag film representing the NRs of *A1–A5@Au*. As shown in Fig. 5a, the configuration for the FDTD simulations involved the Si wafer (thickness of 400 nm), an Ag layer (thickness of 660 nm), a ZnO seed layer (thickness of 20 nm), a hexagonal ZnO prism (height of 1.1 μm and diameter of 155, 205, 240, 349, and 435 nm for the five cases, respectively), and the surrounding medium (air). Total-field scattered-field source polarizing along the *x*-axis with a radiation wavelength of 785 nm was applied on the top of the NRs with the incidence direction along the *z*-axis. The simulated $|E|$ distribution on an *x*–*y* plane for the five different NRs is presented in Fig. 5b and S4. Based on the simulations, $|E|$ along *x*-axis of the NRs and the evanescent field at the ZnO/air interface ($E_{interface}$) were derived (Fig. 5c and d). It was revealed that $E_{interface}$ can be evidently varied by the NRs' average diameter; when the diameter increased from 155 to 435 nm, the simulated $E_{interface}$ first increased and then decreased, delivering the highest $E_{interface}$ by the NR with the diameter of 349 nm (corresponding to the case of *A4@Au*) upon 785 nm excitation. The results not only interpreted the best SERS detection performance of *A4@Au* among the five distinct substrates in the experiments (Fig. 3b), but also emphasized the crucial role of the evanescent field to SERS detection.

As the evanescent field is also associated with the wavelength of the incident light, we further explored the evanescent field by FDTD simulations upon an alternative excitation wavelength (532 nm), using the same structural configuration as in Fig. 5a. Due to the varied excitation wavelength, the NR with diameter of 240 nm (corresponding to the case of *A3@Au* NRs) instead of the NR with diameter of 349 nm (corresponding to the case of *A4@Au* NRs) showed the highest $E_{interface}$ (Fig. S5). We then explored the detection performance of *A1–A5@Au* for R6G upon 532 nm excitation (Figs. S6a and S6b). In good agreement with the simulation results, the performance of *A3@Au* was obviously superior to the rest four substrates. Notably, the peaks of R6G were clearly identified even at a low concentration of 10^{-17} M (Figs. S6c and S6d). Distinct from the ZnO NRs/noble metal NPs-based SERS substrates reported previously (Pal et al., 2019; Du et al., 2022; Zhu et al., 2019; Huang et al., 2015), the design strategy for this present SERS substrate focused on enhancement of evanescent field by optimization of the NRs diameter at a given incident wavelength, combining with the application of the high light-reflection Ag film. The detection concentration (*i.e.*, 10^{-17} M) here is an order of magnitude higher than the best reported detection limit from ZnO NRs/noble metal NPs-based SERS substrates ever reported (Pal et al., 2019; Du et al., 2022; Zhu et al., 2019; Huang et al., 2015). All these experimental and theoretical results further confirmed the key role of the evanescent field to the SERS detection.

Besides the evanescent field, selective capture of the SARS-CoV-2 spike protein also plays a crucial role for the high detection sensitivity in untreated saliva. As shown in the experiments (Fig. 3d and 4b), before MET modification, *A4@Au* substrate can only detect the signals from saliva; after the modification, *A4@MET-Au* delivered significant Raman peaks of SARS-CoV-2 spike protein meanwhile prevented the interference of saliva. To demonstrate the selective capture of SARS-CoV-2 spike protein by MET coating more quantitatively, PCA was performed on SERS spectra (40 spectra collected randomly on the samples) of the untreated saliva with/without SARS-CoV-2 spike protein. Based on the obtained 95% confidence ellipse, the domain of saliva containing SARS-CoV-2 spike protein and that of pristine saliva overlapped in large proportion when using *A4@Au* (Fig. 5e), but completely separated from each other when using *A4@MET-Au* (Fig. 5f).

The selective capture capacity of MET is closely associated with the isoelectric point at a given pH value. It has been demonstrated that the surface charge of proteins is related to the difference between the isoelectric point of the proteins and the pH value of the solution (Hartvig et al., 2011): when the former is identical to the latter, no surface charge can be found on the proteins; when the former is higher (lower) than the latter, the proteins would then positively (negatively) charged. In the present case, the pH value of untreated saliva was measured to be ~6.7. The identified common organic components of untreated saliva (such as mucin, collagen, proline-rich protein, cysteine-rich protein and amylase) in Fig. 3d all showed an isoelectric point smaller than 6.5 (Malamud and Drysdale, 1978; Johnsson et al., 1993; Maslennikova et al., 2013; Isemura et al., 1984; Bansil and Turner, 2006), so that all of them are slightly negatively charged in saliva. In contrast, the SARS-CoV-2 spike protein has an isoelectric point of 7.8 (Krebs et al., 2021) hence being positively charged in saliva. The negatively-charged SERS substrate surface by MET modification can thus efficiently

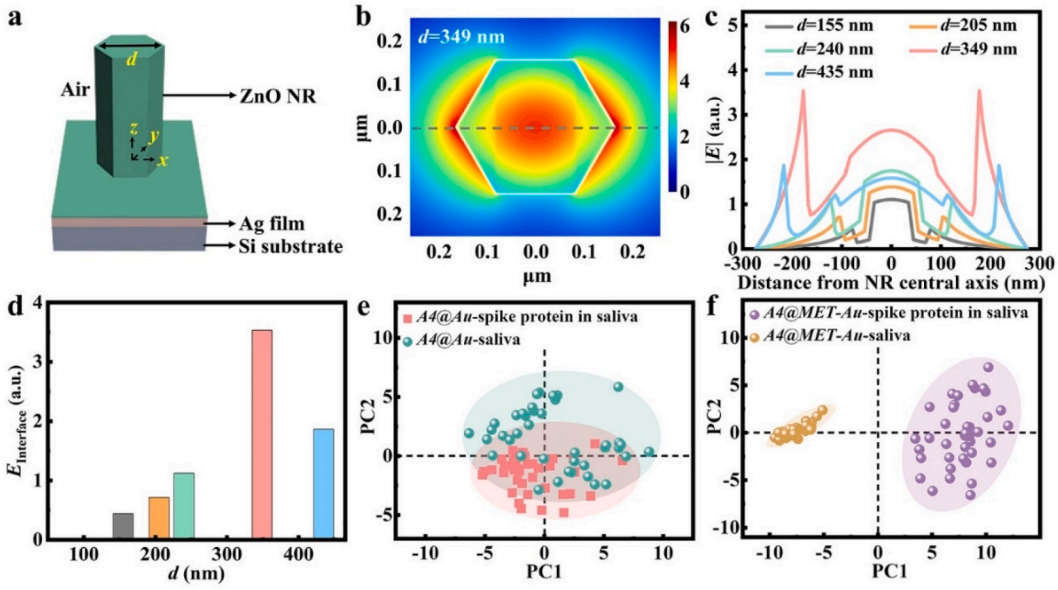

Fig. 5. Mechanism for the ultrasensitive and anti-interference SERS detection. (a) The configuration of ZnO NR on the Ag film-Si wafer for FDTD simulations. (b) The calculated distribution of the electric field $|E|$ on an *x*–*y* plane of a single NR with a diameter of 349 nm. (c) The calculated $|E|$ along *x*-axis of the NRs and (d) evanescent field at the ZnO/air interface with NRs' diameter of 155, 205, 240, 349, and 435 nm, where the radiation wavelength is 785 nm. PCA scatter plots of the pristine and SARS-CoV-2 spike protein-containing saliva with 95% confidence ellipse by using (e), *A4@Au*, and (f), *A4@MET-Au* substrate.

distinguish and capture the viral protein in saliva.

Finally, we explored the detection reproducibility of the SERS substrates. By analyzing twenty SERS spectra collected from randomly-selected detection areas on the substrates, a low relative standard deviation (RSD) value of 6.00% was deduced for R6G detection by using *A3@Au* substrate upon 532 nm excitation (Figs. S6e and S6f). For the detection of SARS-CoV-2 spike protein in PBS and in untreated saliva by using *A4@MET-Au* upon 785 nm excitation, low RSD values of 7.11% and 7.57% were obtained by analyzing ten spectra of randomly-selected areas, respectively (Fig. S7). The reproducibility was not only demonstrated by the spectra obtained from the different areas of a single SERS substrate but also by the results from different substrates (Fig. S8). Reproducible results could be obtained from different batch of the substrates. All these results confirmed the reliable detection reproducibility of the SERS substrates.

5. Conclusions

Based on the combination of strong evanescent field and selective capturing of targeted protein by an antibody- and aptamer-free SERS substrate, *i.e.*, vertically-aligned ZnO NRs arrays on an Ag film where the NRs' sidewalls are decorated with MET-ligands coated Au NPs, ultrasensitive and anti-interference detection of SARS-CoV-2 spike protein in untreated saliva has been realized. The resultant detection limits for SARS-CoV-2 spike protein detection are 3.6×10^{-17} M in PBS and 1.6×10^{-16} M in untreated saliva, which are not only three orders of magnitude improved than the best records from antibody- and aptamer-free SERS substrates (1.3×10^{-13} M in PBS (Luo et al., 2023) and 5.6×10^{-13} M in saliva (Wu et al., 2022)), but also comparable to the best records ever reported from all SERS substrates (1.1×10^{-17} M in PBS and 8.6×10^{-17} M in saliva (Zhang et al., 2021)). Excitingly, the present detection limits are also superior to the best detection limits in body fluids based on other detection strategies reported so far (Table S5). As the first example to gain the high SERS detection sensitivity by the strong evanescent field from the high-order waveguide modes of ZnO NRs, this work unlocks an exciting route to design and fabricate SERS substrates based on various well-defined NRs (*e.g.*, Si NRs and titanium dioxide NRs) for high-performance detection. Meanwhile, the selective capturing of thiolates with specific terminal groups matching the targeted microbial proteins and antigens enriches the tools for highly-selective and anti-interference detection in body fluids, replacing high-cost antibody/aptamer modification of SERS substrates. The anti-interference detection based on the isoelectric point may be extended to selective detection of other targeted proteins in body fluids when their isoelectric point is larger than the pH of the fluids whilst that of the interference components is lower. The importance of such ultrasensitive and anti-interference sensing based on the facile, low-cost techniques is not limited to the clinical applications and epidemic control, but also lies in the broad prospect on high-standard detection of water sources, beverages and food.

CRediT authorship contribution statement

Hong Zhang: Conceptualization, Methodology, Data curation, PCA analysis, FDTD simulations, Writing – original draft. **Chenggang Zhang:** PCA analysis. **Zhaotong Wang:** FDTD simulations. **Wenwu Cao:** Validation. **Miao Yu:** Supervision, Funding acquisition, Writing – review & editing. **Ye Sun:** Conceptualization, Supervision, Funding acquisition, Writing – review & editing.

Declaration of competing interest

The authors declare that they have no known competing financial interests or personal relationships that could have appeared to influence the work reported in this paper.

Data availability

Data will be made available on request.

Acknowledgements

This work was financially supported by the National Natural Science Foundation of China (52073074, 22272041) and State Key Laboratory of Urban Water Resource and Environment (2021TS08).

Appendix A. Supplementary data

Supplementary data to this article can be found online at https://doi.org/10.1016/j.bios.2023.115457.

References

Antoine, D., Mohammadi, M., Vitt, M., Dickie, J.M., Jyoti, S.S., Tilbury, M.A., Johnson, P.A., Wawrousek, K.E., Wall, J.G., 2022. ACS Sens. 7 (3), 866–873.
Bansil, R., Turner, B.S., 2006. Curr. Opin. Colloid Interface Sci. 11 (2–3), 164–170.
Bistaffa, M.J., Camacho, S.A., Pazin, W.M., Constantino, C.J.L., Oliveira Jr., O.N., Aoki, P.H.B., 2022. Talanta 244, 123381.
Börner, S., Rüter, C.E., Voss, T., Kip, D., Schade, W., 2007. Phys. Status Solidi 204 (10), 3487–3495.
Chang, Y.L., Lai, I.C., Lu, L.C., Chang, S.W., Sun, A.Y., Wan, D., Chen, H.L., 2022. Biosens. Bioelectron. 200, 113920.
Cui, F., Zhou, H.S., 2020. Biosens. Bioelectron. 165, 112349.
Daoudi, K., Ramachandran, K., Alawadhi, H., Boukherroub, R., Dogheche, E., Khakani, M.A.E., Gaidi, M., 2021. Surface. Interfac. 27, 101454.
Ding, S., Yi, J., Li, J., Ren, B., Wu, D., Panneerselvam, R., Tian, Z.Q., 2016. Nat. Rev. Mater. 1 (6), 16021.
Du, B., Tang, C., Zhao, D., Zhang, H., Yu, D., Yu, M., Balram, K.C., Gersen, H., Yang, B., Cao, W., Gu, C., Besenbacher, F., Li, J., Sun, Y., 2019. Nanoscale 11 (30), 14322–14329.
Du, B., Tan, J., Ji, C., Shao, M., Zhao, X., Yu, J., Zhang, C., Chen, C., Pan, H., Man, B., Li, Z., 2022. Nano Res. https://doi.org/10.1007/s12274-022-5253-y.
Fiedorova, K., Augustynek, M., Kubicek, J., Kudrna, P., Bibbo, D., 2022. Biosens. Bioelectron. 211, 114348.
Gu, M., Guan, P., Xu, S., Li, H., Kou, Y., Lin, X., Kathiresan, M., Song, Y., Zhang, Y., Jin, S., Li, J.F., 2023. J. Chem. Phys. 158 (2), 024203.
Hartvig, R.A., van de Weert, M., Ostergaard, J., Jorgensen, L., Jensen, H., 2011. Langmuir 27 (6), 2634–2643.
Huang, J., Chen, F., Zhang, Q., Zhan, Y., Ma, D., Xu, K., Zhao, Y., 2015. ACS Appl. Mater. Interfaces 7 (10), 5725–5735.
Isemura, S., Saitoh, E., Sanada, K., 1984. J. Biochem. 96 (2), 489–498.
Johnson, M., 2012. Mater. Methods 2, 120.
Johnsson, M., Levine, M.J., Nancollas, G.H., 1993. Crit. Rev. Oral Biol. Med. 4 (3–4), 371–378.
Kevadiya, B.D., Machhi, J., Herskovitz, J., Oleynikov, M.D., Blomberg, W.R., Bajwa, N., Soni, D., Das, S., Hasan, M., Patel, M., Senan, A.M., Gorantla, S., McMillan, J., Edagwa, B., Eisenberg, R., Gurumurthy, C.B., Reid, S.P.M., Punyadeera, C., Chang, L., Gendelman, H.E., 2021. Nat. Mater. 20 (5), 593–605.
Kim, W., Lee, S.H., Kim, J.H., Ahn, Y.J., Kim, Y.H., Yu, J.S., Choi, S., 2018. ACS Nano 12 (7), 7100–7108.
Krebs, F., Scheller, C., Grove-Heike, K., Pohl, L., Watzig, H., 2021. Electrophoresis 42 (6), 687–692.
Li, D., Zhang, Z., Wang, X., Wang, Y., Gao, X., Li, Y., 2021. Biosens. Bioelectron. 200, 113907.
Long, G.L., Winefordner, J.D., 1983. Anal. Chem. 55 (7), 712–724.
Lukose, J., Chidangil, S., George, S.D., 2021. Biosens. Bioelectron. 178, 113004.
Luo, X., Yue, W., Zhang, S., Liu, H., Chen, Z., Qiao, L., Wu, C., Li, P., He, Y., 2023. Lab Chip 23 (2), 388–399.
Macchia, E., Torricelli, F., Bollella, P., Sarcina, L., Tricase, A., Franco, C.D., Österbacka, R., Kovacs-Vajna, Z.M., Scamarcio, G., Torsi, L., 2022. Chem. Rev. 122 (4), 4636–4699.
Mak, G.C.K., Lau, S.S.Y., Wong, K.K.Y., Chow, N.L.S., Lau, C.S., Lam, E.T.K., Ng, K.H.L., Chan, R.C.W., 2022. Future Virol. 17 (6), 387–392.
Malamud, D., Drysdale, J.W., 1978. Anal. Biochem. 86 (2), 620–647.
Maslennikova, A.D., Sergeeva, I.A., Petrova, G.P., 2013. Moscow univ. Phys. Bull. 68 (2), 154–158.
Ohayon, D., Nikiforidis, G., Savva, A., Giugni, A., Wustoni, S., Palanisamy, T., Chen, X., Maria, I.P., Fabrizio, E.D., Costa, P.M.F.J., McCulloch, I., Inal, S., 2020. Nat. Mater. 19 (4), 456–463.
Pal, A.K., Pagal, S., Prashanth, K., Chandra, G.K., Umapathy, S., Mohan, D.B., 2019. Sens. Actuators, B 279, 157–169.
Parvu, V., Gary, D.S., Mann, J., Lin, Y.C., Mills, D., Cooper, L., Andrews, J.C., Manabe, Y. C., Pekosz, A., Cooper, C.K., 2021. Front. Microbiol. 12, 714242.
Pavia, C.S., Plummer, M.M., 2021. J. Microbiol. Immunol. Infect. 54 (5), 776–786.
Peng, Y., Lin, C., Long, L., Masaki, T., Tang, M., Yang, L., Liu, J., Huang, Z., Li, Z., Luo, X., Lombardi, J.R., Yang, Y., 2021. Nano-Micro Lett. 13 (1), 52.

Shen, Y., Modha, S., Tsutsui, H., Mulchandani, A., 2021. Biosens. Bioelectron. 171, 112721.
Singh, N.K., Ray, P., Carlin, A.F., Magallanes, C., Morgan, S.C., Laurent, L.C., Aronoff-Spencer, E.S., Hall, D.A., 2021. Biosens. Bioelectron. 180, 113111.
Stanborough, T., Given, F.M., Koch, B., Sheen, C.R., Stowers-Hull, A.B., Waterland, M.R., Crittenden, D.L., 2021. ACS Omega 6 (9), 6404–6413.
Taleghani, N., Taghipour, F., 2021. Biosens. Bioelectron. 174, 112830.
Vecchio, C.D., Daniels, B.C., Brancaccio, G., Brazzale, A.R., Lavezzo, E., Ciavarella, C., Onelia, F., Franchin, E., Manuto, L., Bianca, F., Cianci, V., Cattelan, A.M., Dorigatti, I., Toppo, S., Crisanti, A., 2022. Nat. Commun. 13 (1), 5870.
Voss, T., Svacha, G.T., Mazur, E., 2007. Nano Lett. 7 (12), 3675–3680.
Wang, X., Huang, S.C., Hu, S., Yan, S., Ren, B., 2020. Nat. Rev. Phys. 2 (5), 253–271.
Weissleder, R., Lee, H., Ko, J., Pittet, M.J., 2020. Sci. Transl. Med. 12, eabc1931.
Wu, P., Luo, X., Xu, Y., Zhu, J., Jia, W., Fang, N., Cai, C., Zhu, J.J., 2022. Anal. Chem. 94 (50), 17541–17550.
Xiong, J., Dong, C., Zhang, J., Fang, X., Ni, J., Gan, H., Li, J., Song, C., 2022. Biosens. Bioelectron. 213, 114442.
Yeh, Y.J., Le, T.N., Hsiao, W.W.W., Tung, K.L., Ostrikov, K., Chiang, W.H., 2023. Anal. Chim. Acta 1239, 340651.
Yin, Y., Sun, Y., Yu, M., Liu, X., Jiang, T., Yang, B., Liu, D., Liu, S., Cao, W., 2015. Sci. Rep. 5, 8152.
Yüce, M., Filiztekin, E., Özkaya, K.G., 2021. Biosens. Bioelectron. 172, 112752.
Zhang, B.Y., Yin, P., Hu, Y., Szydzik, C., Khan, M.W., Xu, K., Thurgood, P., Mahmood, N., Dekiwadia, C., Afrin, S., Yang, Y., Ma, Q., McConville, C.F., Khoshmanesh, K., Mitchell, A., Hu, B., Baratchi, S., Ou, J.Z., 2022. Biosens. Bioelectron. 198, 113814.
Zhang, D., Peng, L., Shang, X., Zheng, W., You, H., Xu, T., Ma, B., Ren, B., Fang, J., 2020. Nat. Commun. 11 (1), 2603.
Zhang, F., Wang, X., Zhang, T., Zhang, Z., Gao, X., Li, Y., 2023. J. Phys. Chem. Lett. 14 (1), 88–94.
Zhang, M., Li, X., Pan, J., Zhang, Y., Zhang, L., Wang, C., Yan, X., Liu, X., Lu, G., 2021. Biosens. Bioelectron. 190, 113421.
Zhu, Q., Xu, C., Wang, D., Liu, B., Qin, F., Zhu, Z., Liu, Y., Zhao, X., Shi, Z., 2019. J. Mater. Chem. C 7 (9), 2710–2716.